A meshless boundary method for Stokes flows with particles: Application to canalithiasis

F. Boselli[*,†], D. Obrist and L. Kleiser

Institute of Fluid Dynamics , ETH Zurich, 8092 Zurich, Switzerland

SUMMARY

We propose to couple the method of fundamental solutions (MFS) to the force coupling method (FCM). The resulting method is an efficient, easy to program, meshless method for flows at low Reynolds numbers with finite-size particles. In such an approach, the flow domain is extended across the solid particle phase, and the flow is approximated by a superposition of singular Stokeslets positioned outside the flow domain and finite-size multipoles collocated with the particle. To improve the efficiency of the coupling, we propose new MFS quadratures for the computation of the volume integrals required for the FCM. These are exact and do not require the expensive evaluation of Stokeslets. The proposed method has been developed in the context of investigations of the fluid dynamics of canalithiasis, that is, a pathological condition of the semicircular canals of the inner ear. Numerical examples are presented to illustrate the applicability of the method. Copyright © 2013 John Wiley & Sons, Ltd.

1. INTRODUCTION

The semicircular canals (SCCs) are the primary human sensors for angular velocity and are located in the vestibular system that is part of the inner ear. During head rotations, the endolymph, a fluid that fills the SCCs, lags the motion of the canal such that it displaces an elastic sensory structure, the cupula, which transduces the deflection to afferent nerve signals (e.g., [1–3]). Canalithiasis is a pathological condition in which free-floating particles in the SCC disturb the endolymph flow. This is believed to cause benign paroxysmal positional vertigo (BPPV), arguably the most common form of vertigo in humans [4, 5].

Even though the basic mechanisms responsible for BPPV have been extensively discussed in the medical community, only a few studies addressed the problem from a mechanical point of view (e.g., [6–9]). It is the merit of these models to have revealed the basic mechanisms of BPPV with canalithiasis. However, they share several limitations. They do not account for the hydrodynamic interaction between particles but model particle clusters as single heavy particles accounting for the mass of the whole cluster. Also, they assume the particle radius a_p to be very small with respect to the canal lumen (e.g., $a_p = 1 - 15 \,\mu m$), whereas in vivo experiments suggest that the particle lump should be bigger to elicit vertigo (e.g., $20-50 \,\mu m$, [10, 11]). Therefore, these models are not appropriate, for example, to study phenomena such as BPPV fatigue, that is, an attenuation of the vertigo with repeated head maneuvers, which possibly is related to the disintegration of large particle clusters.

---

*Correspondence to: F. Boselli, Institute of Fluid Dynamics, ETH Zurich, 8092 Zurich, Switzerland.
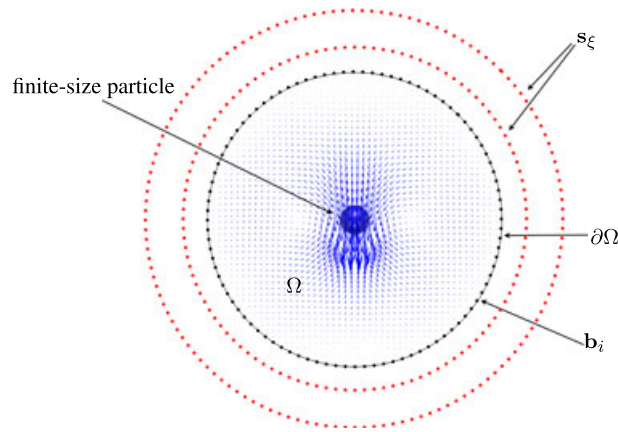[†]E-mail: boselli@ifd.mavt.ethz.ch

Figure 1. MFS source points $\mathbf{s}_\xi$ positioned on two layers at different distances from the boundary $\partial\Omega$ of the flow domain Ω containing a force coupling method particle; MFS collocation points $\mathbf{b}_i$ on $\partial\Omega$. The particle volume is occupied by fluid, and no collocation point is positioned on the particle surface.

To overcome these limitations, we have developed a new coupling between the method of fundamental solutions (MFS) and the force coupling method (FCM) that we propose here from a general point of view as a mesh-free method for Stokes flow with finite-size particles. The FCM is an elegant method proposed by Maxey and coworkers [12, 13] to model finite-size particles and their interaction. In such an approach, the fluid domain is extended over the particle volume, and each particle enters the flow equations as a body force in the shape of finite-size multipoles, that is, spherical Gauss functions (force envelopes) that are collocated with the particle center and scale with the particle size. The FCM is efficient because it does not discretize the particle wall. Even though small errors can be observed very close to the wall, the predicted flow field is very close to the exact flow field about a spherical finite-size particle [12].

We found it natural to solve the resulting governing equations by the multilayer MFS [14]. The MFS approximates the flow field as a superposition of Stokeslets with their singularities (source points) positioned outside the flow domain (Figure 1).

The introduction of n_p particles into the flow domain is mathematically equivalent to augmenting the MFS expansion with n_p finite-size multipoles located inside the flow domain.

The FCM and the multilayer MFS are introduced in more detail in Sections 2 and 3, respectively. The MFS–FCM coupling is presented in Section 4 together with new efficient MFS quadratures for the FCM integrals. In the second part of the paper, we present (Sections 5.1 and 5.2) and validate (Section 5.3) a domain-decomposition strategy for the computation of particle-driven flows in a toroidal canal. This strategy can be applied to several kinds of biomedical flows. In Section 5.4, we demonstrate the applicability of such an approach to canalithiasis by means of numerical examples. In Section 6, we make our final remarks and conclude the paper.

2. FORCE COUPLING METHOD

The FCM was first proposed in [12] and then refined in [13]. Several publications have established the FCM as an efficient and reliable method for the study of sedimentation of spherical particles [15–17] and their behavior in Poiseuille flows [18]. Moreover, the FCM is of great interest in the context of paramagnetic particles [19, 20] and was applied for the modeling and the design of micro-pumps [21] and micro-swimmers [22]. The FCM was mainly studied in the context of spherical particles, but it can easily be extended for the treatment of ellipsoidal particles [23].

Although the FCM can be used with the full Navier–Stokes equations, here we consider the Stokes flow equations

$$-\nabla p(\mathbf{x}, t) + \mu \nabla^2 \mathbf{u}(\mathbf{x}, t) = \mathbf{f}(\mathbf{x}, t) \tag{1a}$$

$$\nabla \cdot \mathbf{u}(\mathbf{x}, t) = 0, \tag{1b}$$

where $\mathbf{u} = (u_1, u_2, u_3)$ and p are the velocity and the pressure of the fluid, and $\mathbf{x} = (x_1, x_2, x_3)$ are the Cartesian coordinates. The flow domain is extended over the particle volume, and the particles enter the flow equations (1) as the body force $\mathbf{f} = \{\sum_{\xi=1}^{n_p} f_i^{(\xi)}\}$, where n_p is the number of particles. The contribution $f_i^{(\xi)}$ of the ξth particle to $\mathbf{f}$ in the ith coordinate direction is approximated by a finite-size multipole expansion,

$$f_i^{(\xi)}(\mathbf{x}, t) \approx \underbrace{-F_i^{(\xi)} \Delta_M(\mathbf{x} - \mathbf{Y}_\xi(t))}_{\text{monopole}} \underbrace{- G_{ij}^{(\xi)} \frac{\partial}{\partial x_j} \Delta_D(\mathbf{x} - \mathbf{Y}_\xi(t))}_{\text{dipole}}, \tag{2}$$

where Δ_M and Δ_D are spherical Gauss functions called force envelopes, $\mathbf{Y}_\xi$ is the center of the ξth particle, and $F_i^{(\xi)}$ and $G_{ij}^{(\xi)}$ are the monopole and dipole coefficients, respectively [12, 13].

The first-order term of (2) is a finite-size monopole. The strength $F_i^{(\xi)}$ is given by the sum of the volumetric forces acting on the particle (e.g., gravity force) and is distributed over the particle volume by the force envelope Δ_M,

$$\Delta_M(\mathbf{x} - \mathbf{Y}_\xi) := (2\pi\sigma_M^2)^{-3/2} \exp\left[\frac{-(\mathbf{x} - \mathbf{Y}_\xi)^2}{2\sigma_M^2}\right], \tag{3}$$

with the length scale $\sigma_M = a_p/\sqrt{\pi}$ similar to the particle size.

Even though the monopole term alone already gives good predictions of the flow field and the settling velocity of spherical particles [12, 15, 17], one can increase the order of the multipole expansion by adding a dipole [13], that is, the second term of (2). The force envelope Δ_D for the dipole is defined as in (3) but with the length scale $\sigma_D = a_p/(6\sqrt{\pi})^{1/3}$ instead of σ_M. The dipole tensor $G_{ij}^{(\xi)}$ due to the ξth particle can be split into a symmetric part and an antisymmetric part. The antisymmetric part of the dipole represents the external torque $T_i^{(\xi)} = \epsilon_{ijk} G_{jk}^{(\xi)}$ acting on the ξth particle [13], where ϵ_{ijk} is the Levi-Civita symbol. In our specific application, gravity is the only external force, and no torque acts on the particle. Therefore, the antisymmetric part of $G_{ij}^{(\xi)}$ is zero and will not be discussed further. The symmetric part of the dipole (stresslet) represents only internal forces exchanged between the particle and the fluid phase. The symmetric part of $G_{ij}^{(\xi)}$ is chosen by minimizing the average rate of strain $E_{ij}^{(\xi)}$ of the volume of fluid occupied by the ξth particle,

$$E_{ij}^{(\xi)} = \int_{\mathbb{R}^3} \frac{1}{2}\left(\frac{\partial u_i}{\partial x_j} + \frac{\partial u_j}{\partial x_i}\right) \Delta_D(\mathbf{x} - \mathbf{Y}_\xi) d^3\mathbf{x}, \tag{4}$$

which reflects that the contribution of a stresslet to the total rate of work is zero [13]. Several algorithms have been proposed to determine $G_{ij}^{(\xi)}$ [13, 24]. We adopt the recent algorithm proposed in [25]. In a first step, the contribution E_{ij}^M of the monopoles to $E_{ij}^{(\xi)}$ is computed for the value of $F_i^{(\xi)}$ given by the external forces and $G_{ij}^{(\xi)} = 0$. In a second step, the contribution E_{ij}^D of the symmetric dipoles to $E_{ij}^{(\xi)}$ is computed for a first guess of $G_{ij}^{(\xi)}$ and $F_i^{(\xi)} = 0$. Then, the value of $G_{ij}^{(\xi)}$, and with that the value of E_{ij}^D, is updated in a conjugate gradient iteration to satisfy the condition $E_{ij}^M + E_{ij}^D = 0$ [25].

In contrast to more traditional methods, the FCM leads to a mobility formulation of the problem; that is, we impose the force $F_i^{(\xi)}$ for each particle, and the FCM returns the particle velocity. To do this, the governing equations are solved with an appropriate body force $\mathbf{f}$. The linear velocity $\mathbf{v}^{(\xi)}$ of the ξth particle is then computed as

$$\mathbf{v}^{(\xi)}(t) = \int_{\mathbb{R}^3} \mathbf{u}(\mathbf{x}, t) \Delta_M(\mathbf{x} - \mathbf{Y}_\xi(t)) d^3\mathbf{x}, \tag{5}$$

which gives a local average of the fluid velocity at the particle location. The angular velocity $\Omega_i^{(\xi)}$ of the particle is defined as

$$\Omega_i^{(\xi)}(t) = \int_{\mathbb{R}^3} \epsilon_{ijk} \frac{\partial u_k(\mathbf{x}, t)}{\partial x_j} \Delta_D(\mathbf{x} - \mathbf{Y}_\xi(t)) \mathrm{d}^3 \mathbf{x}, \tag{6}$$

which gives a local average of the vorticity at the particle location. Note that the dipole and monopole strengths do not enter (6), and the particle can rotate without acceleration also for $G_{ij} = 0$ and $F_i = 0$. The definitions (5) and (6), together with the length scales σ_M and σ_D, were chosen to match the linear and angular velocities predicted by the Stokes theory for an isolated particle under the action of a given force F_i and a torque $\epsilon_{ijk} G_{jk}$, respectively. This also ensures a self-consistent kinetic energy budget [12, 13].

3. MULTILAYER METHOD OF FUNDAMENTAL SOLUTIONS

The MFS [26, 27] has been identified as a promising method for the solution of the Stokes flow equations [28–33]

$$-\nabla p_{\mathrm{h}} + \mu \nabla^2 \mathbf{u}_{\mathrm{h}} = 0 \tag{7a}$$
$$\nabla \cdot \mathbf{u}_{\mathrm{h}} = 0, \tag{7b}$$

where the subscript h indicates that (7) is a homogeneous equation. The flow field $\mathbf{u}_{\mathrm{h}}$ and the pressure p_{h} are approximated by an expansion of N_{s} Stokeslets with source points $\mathbf{s}_\xi$ located outside the flow domain Ω (Figure 1),

$$\mathbf{u}_{\mathrm{h}}(\mathbf{x}) \approx \sum_{\xi=1}^{N_{\mathrm{s}}} \mathbf{S}(\mathbf{x} - \mathbf{s}_\xi) \mathbf{w}_\xi \tag{8a}$$

$$p_{\mathrm{h}}(\mathbf{x}) \approx \sum_{\xi=1}^{N_{\mathrm{s}}} \mathbf{\Pi}(\mathbf{x} - \mathbf{s}_\xi) \mathbf{w}_\xi \tag{8b}$$

where $\mathbf{w}_\xi = \{w_{\xi,j}\}$ is the strength of the Stokeslet associated with the ξth source point, and $\mathbf{S} = \{S_{ij}\}$ and $\mathbf{\Pi} = \{\Pi_j\}$ are the velocity and pressure Stokeslet tensors, respectively. In three dimensions, we have [34]

$$S_{ij}(\hat{\mathbf{x}}) = \frac{1}{8\pi\mu} \left[\frac{1}{r} \delta_{ij} + \frac{\hat{x}_i \hat{x}_j}{r^3} \right] \tag{9}$$

$$\Pi_j(\hat{\mathbf{x}}) = \frac{1}{4\pi} \frac{\hat{x}_j}{r^3} \tag{10}$$

with $\hat{\mathbf{x}} = \{\hat{x}_i\} = \mathbf{x} - \mathbf{s}_\xi$, $r = |\hat{\mathbf{x}}|$, and δ_{ij} the Kronecker delta.

A Stokeslet satisfies (1) with $\mathbf{f} = -\mathbf{w}_\xi \delta(\hat{\mathbf{x}})$, where $\delta(\hat{\mathbf{x}})$ is the Dirac delta function. Therefore, it also satisfies the homogeneous Stokes equations (7) everywhere except at $\mathbf{x} = \mathbf{s}_\xi$. If we assume the coordinates $\mathbf{s}_\xi$ to be known, then the unknowns in the MFS expansion (8) are the source strengths $\mathbf{w}_\xi$ that can be determined by enforcing boundary conditions at a certain number M_{c} of collocation points $\mathbf{b}_i$ (Figure 1). This leads to a linear system of equations that can be expressed in matrix form as

$$\mathbf{A}\mathbf{w} = \mathbf{g} \tag{11}$$

where the entries of the ξth column of $\mathbf{A}$ are evaluations of the ξth Stokeslet at the collocation points $\mathbf{b}_i$, $\mathbf{w} = \{\mathbf{w}_\xi\}$ is the vector of the unknown Stokeslet strengths, and $\mathbf{g}$ is the vector describing the boundary conditions at the collocation points.

The stability and the accuracy of the MFS depend on the position of the source points. Previous implementations of the MFS (monolayer MFS) considered source points positioned on a single

layer with an arbitrary distance from the boundary. Recent works [14, 35–37] have shown that positioning the source points on multiple layers by greedy algorithms improves the accuracy and the convergence rate of the MFS and its robustness with respect to the user-defined source layers. We consider here the multilayer MFS proposed in [14] for Stokes flow problems. The source points are positioned on several layers at different distances from the boundary (Figure 1), and the linear system (11) is solved in the least-squares sense by the block greedy-QR algorithm (BGQRa) proposed in [14]. The BGQRa selects $N < 3M_c$ appropriate columns of $\mathbf{A}$ to obtain a $3M_c \times N$ suboptimal submatrix $\mathbf{A}^{\text{opt}}$ that is then used instead of the full matrix $\mathbf{A}$ for computing the least-squares solution of (11). Increasing the distance of the source layer from the boundary tends to increase the convergence rate of the monolayer MFS, but it decreases the attainable accuracy as well. This leads to an unfavorable compromise between attainable accuracy and convergence rate. The BGQRa overcomes this limitation by resolving the coarse scales of the solution with a distant source layer and by iteratively introducing closer layers to resolve the finer scales. This allows to combine the high convergence rate attainable for distant sources with the high accuracy attainable for close sources [14, 38]. The matrix $\mathbf{A}$ is divided into blocks of columns such that each block corresponds to a given source layer, and only the columns associated with the current block need to be allocated in memory. This reduces the operation count and the memory required by the BGQRa compared with other greedy algorithms that process the full matrix $\mathbf{A}$ at a time.

4. COUPLING THE METHOD OF FUNDAMENTAL SOLUTIONS TO THE FORCE COUPLING METHOD

We couple the MFS to the FCM in order to solve (1) with no-slip boundary conditions at the solid boundaries $\partial\Omega$ of the fluid domain Ω,

$$\mathbf{u}|_{\partial\Omega} = 0. \tag{12}$$

Because (1) is a linear equation, we can split $\mathbf{u}$ into a particular solution $\mathbf{u}_{\text{p}}$ and a homogeneous solution $\mathbf{u}_{\text{h}}$. The particular solution does not need to satisfy the boundary conditions and is evaluated as

$$\mathbf{u}_{\text{p}}(\mathbf{x}) = \sum_{\xi=1}^{n_{\text{p}}} \left[\mathbf{u}_M(\mathbf{x} - \mathbf{Y}_\xi) + \mathbf{u}_D(\mathbf{x} - \mathbf{Y}_\xi) \right], \tag{13}$$

where $\mathbf{u}_M$ and $\mathbf{u}_D$ are exact solutions of the Stokes equations (1) for $\mathbf{f} = \{-F_i^{(\xi)} \Delta_M(\mathbf{x} - \mathbf{Y}_\xi)\}$ (monopole) and $\mathbf{f} = \{-G_{ij}^{(\xi)} \frac{\partial}{\partial x_j} \Delta_D(\mathbf{x} - \mathbf{Y}_\xi)\}$ (dipole), respectively. The flow $\mathbf{u}_M = \{u_{M,i}\}$ due to an isolated monopole represents the flow of a particle settling in an otherwise quiescent fluid and was shown [12] to have the form

$$u_{M,i}(\mathbf{x}) = \hat{S}_{ij}(\hat{\mathbf{x}}) F_j, \tag{14}$$

$$\hat{S}_{ij} = A_M(r)\delta_{ij} + B_M(r)\hat{x}_i \hat{x}_j, \tag{15}$$

where $\hat{\mathbf{x}} = \{\hat{x}_i\} = \mathbf{x} - \mathbf{Y}_\xi$, $r = |\hat{\mathbf{x}}|$, and

$$A_M(r) = \frac{1}{8\pi\mu r} \left[\left(1 + \frac{\sigma_M^2}{r^2}\right) \text{erf}\left(\frac{r}{\sigma_M \sqrt{2}}\right) - \frac{2\sigma_M}{r\sqrt{2\pi}} \exp\left(-\frac{r^3}{2\sigma_M^2}\right) \right], \tag{16}$$

$$B_M(r) = \frac{1}{8\pi\mu r^3} \left[\left(1 - \frac{3\sigma_M^2}{r^2}\right) \text{erf}\left(\frac{r}{\sigma_M \sqrt{2}}\right) + \frac{6\sigma_M}{r\sqrt{2\pi}} \exp\left(-\frac{r^3}{2\sigma_M^2}\right) \right]. \tag{17}$$

The flow $\mathbf{u}_D = \{u_{D,i}\}$ due to an isolated symmetric dipole represents the flow disturbance induced by placing a solid particle in the external straining flow $u_i = E_{ij} x_j$ and has the form [13]

$$u_{D,i}(\mathbf{x}) = R_{ijk}(\hat{\mathbf{x}}) G_{jk}, \tag{18}$$

$$R_{ijk} = \frac{\mathrm{d}A_D}{\mathrm{d}r}\delta_{ij}\hat{x}_k/r + B_D(r)(\delta_{ik}\hat{x}_j + \delta_{jk}\hat{x}_i) + \frac{\mathrm{d}B_D}{\mathrm{d}r}\hat{x}_i\hat{x}_j\hat{x}_k/r, \tag{19}$$

where A_D and B_D are defined as in (16) and (17) but with the length scale σ_D instead of σ_M.

The homogeneous solution $\mathbf{u}_\mathrm{h}$ is computed by the multilayer MFS with the boundary conditions $\mathbf{u}_\mathrm{h}|_{\partial\Omega} = -\mathbf{u}_\mathrm{p}|_{\partial\Omega}$. The sought solution $\mathbf{u} = \{u_i\}$ can then be simply evaluated as the augmented MFS expansion

$$u_i(\mathbf{x}) = \underbrace{\sum_{\xi=1}^{N_\mathrm{s}} S_{ij}(\mathbf{x}-\mathbf{s}_\xi)w_{\xi,j}}_{\mathbf{u}_\mathrm{h}} + \underbrace{\sum_{\xi=1}^{n_\mathrm{p}}\left[\hat{S}_{ij}(\mathbf{x}-\mathbf{Y}_\xi)F_j^{(\xi)} + R_{ijk}(\mathbf{x}-\mathbf{Y}_\xi)G_{jk}^{(\xi)}\right]}_{\mathbf{u}_\mathrm{p}} \tag{20}$$

and satisfies $\mathbf{u}|_{\partial\Omega} = 0$.

4.1. Computation of the force coupling method integrals

It is convenient to compute the contributions of the particular and homogeneous solutions to the particle velocity (5), angular velocity (6), and fluid rate of strain (4) independently. The integrals of the particular solution $\mathbf{u}_\mathrm{p}$ can be efficiently approximated by a Gauss–Hermite quadrature. For example, the contribution of $\mathbf{u}_\mathrm{p}$ to the velocity of a particle ξ is

$$\int_{\mathbb{R}^3}\mathbf{u}_\mathrm{p}(\mathbf{x})\Delta_M(\mathbf{x}-\mathbf{Y}_\xi)\mathrm{d}^3\mathbf{x} \approx \pi^{-3/2}\sum_{i=1}^{n_g}\sum_{j=1}^{n_g}\sum_{k=1}^{n_g}\lambda_i\lambda_j\lambda_k\mathbf{u}_\mathrm{p}(\tilde{\mathbf{x}}_{ijk}+\mathbf{Y}_\xi), \tag{21}$$

where n_g is the number of quadrature nodes, λ_q are the weights of the quadrature, and $\tilde{\mathbf{x}}_{ijk}$ is the vector $\sqrt{2}\sigma(\tilde{x}_i, \tilde{x}_j, \tilde{x}_k)$ with $\tilde{x}_q$ the roots of the Hermite polynomial of order n_g. The values of $\tilde{x}_q$ and λ_q are tabulated in [39]. The integrals (6) and (4) of $\mathbf{u}_\mathrm{p}$ can be approximated by Gauss–Hermite quadratures similar to (21). Computing Gauss–Hermite quadratures also for the homogeneous solution $\mathbf{u}_\mathrm{h}$ would require the evaluation of N_s Stokeslets at n_g^3 integration points (i.e., on the order of $N_\mathrm{s}n_g^3$ operations) at each time step. Therefore, we propose a more efficient approach that is based on the reciprocal theorem [34, 40] and does not require to evaluate the MFS expansion. In this new approach (as derived in Appendix A), the contribution of $\mathbf{u}_\mathrm{h}$ to the FCM integrals becomes

$$\int_{\mathbb{R}^3}u_{\mathrm{h},i}(\mathbf{x})\Delta_M(\mathbf{x}-\mathbf{Y}_\xi)\mathrm{d}^3\mathbf{x} = \sum_{\kappa=1}^{N_\mathrm{s}}\hat{S}_{ik}(\mathbf{s}_\kappa-\mathbf{Y}_\xi)w_{\kappa,k}, \tag{22a}$$

$$\int_{\mathbb{R}^3}\epsilon_{ijl}\frac{\partial u_{\mathrm{h},l}}{\partial x_j}\Delta_D(\mathbf{x}-\mathbf{Y}_\xi)\mathrm{d}^3\mathbf{x} = -\epsilon_{ijl}\sum_{\kappa=1}^{N_\mathrm{s}}R_{klj}(\mathbf{s}_\kappa-\mathbf{Y}_\xi)w_{\kappa,k}, \quad \text{and} \tag{22b}$$

$$\int_{\mathbb{R}^3}\frac{1}{2}\left(\frac{\partial u_{\mathrm{h},i}}{\partial x_j}+\frac{\partial u_{\mathrm{h},j}}{\partial x_i}\right)\Delta_D(\mathbf{x}-\mathbf{Y}_\xi)\mathrm{d}^3\mathbf{x} = -\frac{1}{2}\sum_{\kappa=1}^{N_\mathrm{s}}[R_{kij}(\mathbf{s}_\kappa-\mathbf{Y}_\xi)+R_{kji}(\mathbf{s}_\kappa-\mathbf{Y}_\xi)]w_{\kappa,k}, \tag{22c}$$

where (22a), (22b), and (22c) are the contributions of $\mathbf{u}_\mathrm{h}$ to the velocity (5), the angular velocity (6), and the fluid rate of strain (4), respectively. Unlike the Gauss–Hermite quadratures, the 'MFS quadratures' (22) are exact solutions of the FCM integrals. Moreover, the evaluation of (22) requires to evaluate only the tensors $\hat{S}_{ik}$ and R_{ijk} at the N_s source points used by the MFS, which makes this approach approximately n_g^3 times faster than an approximate Gauss quadrature such as (21). In practice, Equation (22) is computed by the evaluation of only the N fundamental solutions selected by the BGQRa instead of all N_s Stokeslets.

5. APPLICATION TO PARTICLE-DRIVEN FLOWS IN A TORUS

We now consider the flow induced by n_p particles settling under the action of gravity in a slender torus with a minor radius a_SCC and a major radius R_SCC such that $a_\mathrm{SCC}/R_\mathrm{SCC} \ll 1$.
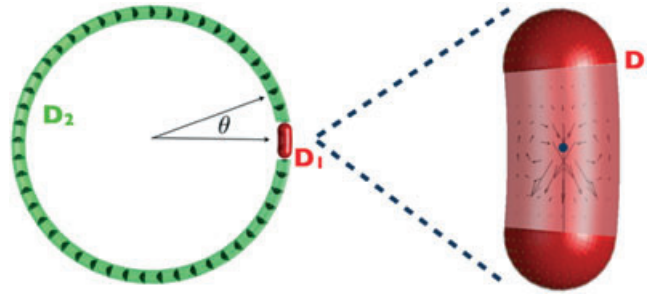
Figure 2. Domain decomposition strategy: The flow field close to the particle (subdomain D_1) is computed numerically. The flow far from the particle (subdomain D_2) is approximated by a Poiseuille flow. The major and minor radii of the torus are $R_{SCC} = 3.64$ mm and $a_{SCC} = 182\mu$m, respectively.

5.1. Domain decomposition

We start by considering only one particle. We split the flow domain into a subdomain D_1 close to the particle and a subdomain D_2 distant from the particle (Figure 2). The interfaces between D_1 and D_2 can be of any shape, and we choose them as semi-spheres (Figure 2). Far away from the particle, the flow can be approximated by a Poiseuille flow.

The flow in D_1 is evaluated by the superposition of a numerical solution and a Poiseuille flow. The numerical solution is obtained by considering D_1 as a closed domain (i.e., no-slip boundary conditions also at the interfaces between D_1 and D_2). It leads to a pressure difference ΔP_p across the two ends of D_1. The flow in D_2 is approximated by a Poiseuille flow with the same flow rate Q as the Poiseuille flow in D_1. The flow rate Q is determined as

$$Q = \Delta P_p / R_h, \tag{23}$$

where R_h is the Poiseuille hydraulic resistance

$$R_h = \frac{8\mu \, \beta \, R_{SCC}}{a_{SCC}^4 \, \pi} \tag{24}$$

with $\beta = 2\pi$ as the angle spanned by the full torus centerline.

5.1.1. Implementation details. During a simulation, a particle moves along the torus, changing its angular position θ. To speed up the simulation, we do not move the subdomain D_1 with the particle. Instead, we map the particle into a fixed auxiliary subdomain D_1 centered around $\theta = 0$ at each time step. This is readily carried out by rotating the position of the particle center and the involved forces by an angle $-\theta$. For example, the flow **u** induced by a monopole of strength F_i and dipole coefficients G_{ij} due to a particle centered at any point $\mathbf{Y} = \{Y_i\}$ in the torus is computed as the flow $\tilde{\mathbf{u}}$ induced by a monopole of strength $\tilde{F}_i$ and dipole coefficients $\tilde{G}_{ij}$ centered at $\tilde{Y}_i$ in the auxiliary computational domain D_1 with

$$\tilde{F}_i = a_{ij}(-\theta)F_j, \tag{25a}$$

$$\tilde{G}_{ij} = a_{im}(-\theta)G_{mk}a_{kj}(\theta), \tag{25b}$$

and

$$\tilde{Y}_i = a_{ij}(-\theta)Y_j, \tag{25c}$$

where $a_{ij}(\theta)$ is the rotation matrix

$$\begin{pmatrix} a_{11} & a_{12} \\ a_{21} & a_{22} \end{pmatrix} = \begin{pmatrix} \cos\theta & -\sin\theta \\ \sin\theta & \cos\theta \end{pmatrix}. \tag{26}$$

The particle velocity $\tilde{v}_i$ and the fluid rate of strain $\tilde{E}_{ij}$ are then computed in D_1 and rotated back by an angle θ to obtain the actual velocity v_i and the rate of strain E_{ij}:

$$v_i = a_{ij}(\theta)\tilde{v}_j, \tag{27a}$$

$$E_{ij} = a_{im}(\theta)\tilde{E}_{mk}a_{kj}(-\theta). \tag{27b}$$

Using a fixed subdomain D_1 makes it possible to use the same collocation points and fundamental solutions at any time step. This allows us to compute the factorization $\mathbf{A}^{\mathrm{opt}} = \mathbf{QR}$ (whose cost scales like N^3) only once and to solve the equivalent system $\mathbf{Rw} = \mathbf{Q}^T\mathbf{g}$ for the other computations. This way, the dominant work is limited to the update of the boundary conditions and the inversion of the upper triangular matrix $\mathbf{R}$ that scales like N^2.

5.2. Far-field pressure due to multipoles in a long tube

The pressure difference ΔP_p that is required to compute the flow rate (23) could be simply obtained by evaluating the pressure form of the modified MFS expansion (20) at the two ends of the subdomain D_1. This can be computationally expensive because it requires the evaluation of N fundamental solutions. We can save computational time by approximating ΔP_p by the analytical solution of the pressure difference induced by a finite-size monopole and a dipole between the two ends of an infinitely long pipe. To find this analytical solution, we apply the reciprocal theorem again and extend the derivation by Squires *et al.* [8] for a Stokeslet to finite-size multipoles (Appendix B). We obtain

$$\Delta P_\mathrm{p} \approx \frac{2F_{\|}}{a_{\mathrm{SCC}}^2 \pi} \int_\Omega \left(1 - \frac{b^2}{a_{\mathrm{SCC}}^2}\right) \Delta_M(\hat{\mathbf{x}})\mathrm{d}\Omega$$
$$- \frac{2G_{ij}e_i}{a_{\mathrm{SCC}}^2 \pi} \int_\Omega \left(1 - \frac{b^2}{a_{\mathrm{SCC}}^2}\right) \frac{\hat{x}_j}{\sigma_D^2} \Delta_D(\hat{\mathbf{x}})\mathrm{d}\Omega \tag{28}$$

where Ω is the fluid volume, b is the distance from the centerline of the torus, $\hat{\mathbf{x}} = \mathbf{x} - \mathbf{Y}$, e_i is the unit vector parallel to the centerline, and $F_{\|} = F_i e_i$. The new expression (28) does not require to evaluate the MFS expansion and can be efficiently computed by a Gauss–Hermite quadrature [39] by setting the velocity $\mathbf{u}$ to zero outside the tube (i.e., for $b > a_{\mathrm{SCC}}$).

It is interesting to note from (28) that the contribution of a monopole (first term) to ΔP_p depends only on the particle position. In contrast, the contribution of the dipole to ΔP_p (second term) is intrinsically related to the flow field via the dependence of G_{ij} on E_{ij}.

Squires *et al.* [8] also discussed the error arising when the curvature of the torus is neglected. This error turns out to be small (about 5%) for the ratios $a_{\mathrm{SCC}}/R_{\mathrm{SCC}}$ that are typical of an SCC.

For simulations with more than one particle, the flow velocity $\mathbf{u}$ and the pressure difference ΔP_p can be obtained as the superposition of the contributions $\mathbf{u}^{(\xi)}$ and $\Delta P_\mathrm{p}^{(\xi)}$ of each particle, where the values for each $\mathbf{u}^{(\xi)}$ and $\Delta P_\mathrm{p}^{(\xi)}$ are computed independently. The mutual dependence between the contribution of each particle is taken into account implicitly by the dipole term.

5.3. Validation against analytical solutions

In what follows, we will consider the results for a subdomain D_1 that spans at least an angle of $3a_{\mathrm{SCC}}/R_{\mathrm{SCC}}$. A similar dimension of the computational domain was also employed by [41] for the computation of the velocity of a particle in a capillary.

If the subdomain D_1 is sufficiently long and the ratio $a_{\mathrm{SCC}}/R_{\mathrm{SCC}}$ sufficiently small, then the numerical solution should approximate the flow induced by a particle in an infinitely long tube such that it can be validated against analytical solutions. Analytical results are available in the limit of a small particle close to the boundary [42] or when the distance of the particle from the wall is bigger than several particle radii [8, 40].

We first present results for a particle radius $a_\mathrm{p}/a_{\mathrm{SCC}} = 0.13$ computed in a subdomain D_1 of a torus with the radii $a_{\mathrm{SCC}} = 182$ μm and $R_{\mathrm{SCC}} = 3.64$ mm (typical values for an SCC). The computed particle velocity and pressure are plotted in Figure 3(a) and 3(b), respectively, as a function of
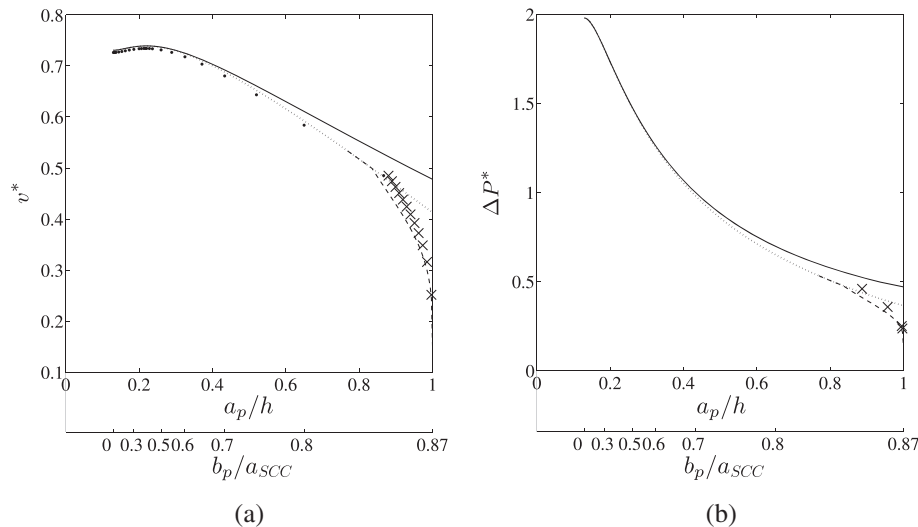
Figure 3. (a) Nondimensional velocity $v^* = |\mathbf{v}|/|\mathbf{W}_{St}|$ and (b) pressure difference $\Delta P^* = \Delta P_p a_{SCC}^2 \pi / F_\parallel$ for a particle of radius $a_p/a_{SCC} = 0.13$ settling in a vertical pipe. $\mathbf{W}_{St}$ is the Stokes settling velocity, h is the particle center to wall distance, and b_p is the particle center to centerline distance. ——, force coupling method (FCM) monopole; · · ·, FCM monopole and dipole; – – –, monopole, dipole, and lubrication force; •, Ref. [40]; ×, Refs [42] and [24]. In (b), theoretical results from [40] and [8] for particles far from the boundary coincide with the pressure due to the monopole (——).

the particle position. The FCM behaves as expected from previous studies that employed volumetric mesh methods.

When the particle is far from the boundary, that is, close to the centerline, the predicted velocity and pressure due to the monopole are in very good agreement with the theoretical results, and it is not necessary to add the dipole term to the FCM expansion (2). When moving the particle toward the wall, the monopole tends to overestimate the particle velocity and the induced pressure difference. Introducing a dipole improves the agreement with the asymptotic results for a particle close to the wall. When the gap between the particle and the wall is less than $0.2a_{SCC}$, it is necessary to introduce the lubrication force proposed in [24] in order to match the theory for spherical particles.

The examples shown earlier were computed with 4643 collocation points. The distance between collocation points near the center of the auxiliary subdomain D_1 was about one-fifth of the particle diameter. Away from this region, their mutual distance was smoothly increased to about one particle diameter. We offered five layers of candidate source points to the BGQRa. The distances of the layers from the boundary were $[2a_{SCC}, 1a_{SCC}, 0.5a_{SCC}, 0.2a_{SCC}, \text{and } a_p]$, and the numbers of source points per layer were $[434, 1083, 3190, 2492, \text{and } 2335]$. When the particle is at the boundary, the BGQRa selects 1468 fundamental solutions out of these candidates. The same set of fundamental solutions could also be used when the particles were away from the wall.

Figure 4 shows the pressure difference predicted by a monopole centered and directed along the centerline of a torus with $R_{SCC} = 3$ mm and $a_{SCC} = 0.16$ mm. The particle size is varied from infinitely small ($a_p \to 0$) to closely fitting ($a_p \to a_{SCC}$). Interestingly, the pressure difference (28) due to the monopole alone leads to accurate results for any particle size. When the particle is small, our predictions match the theory for small particles [8, 40], and when the particle radius is as big as the canal radius, our predictions match the asymptotic theory for a closely fitting particle [43].

The fact that ΔP_p is overestimated by a monopole due to a small sphere close to the boundary (Figure 3(b)) but well predicted for a closely fitting sphere on the centerline (Figure 4) is not intuitive. For intermediate-size particles, the high accuracy of the monopole-based predictions for the particle at the centerline is due to the axisymmetry of the flow profile such that the dipole coefficients are exactly equal to zero. Moreover, the nondimensional pressure difference $\Delta P_p a_{SCC}^2 \pi / F_\parallel$ must be equal to the ratio between the velocity of a neutrally buoyant particle in a Poiseuille flow
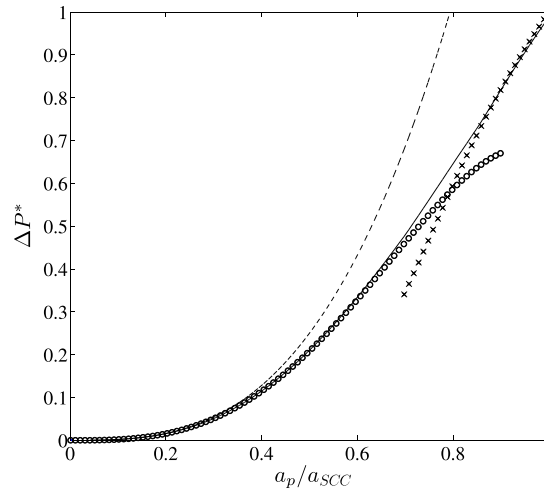
Figure 4. Nondimensional pressure difference $\Delta P^* = \Delta P_p a_{SCC}^2 \pi / F_\parallel$ induced by a particle on the centerline as a function of the particle radius a_p: $---$ and $\circ$, theoretical results for $a_p/a_{SCC} \ll 1$ from [8] (Stokeslet theory), and [40], respectively; $\times$, theory for a closely fitting sphere [43]; ——, force coupling method monopole (Equation 28).

and the mean velocity of the Poiseuille flow [42]. The velocity predicted by (5) for a closely fitting sphere in a Poiseuille flow is approximately the average velocity of the Poiseuille flow. This is the expected result and explains the accurate prediction of ΔP_p for a closely fitting sphere even if the lubrication force is not introduced.

5.4. Multiple particles settling in a toroidal duct

We now consider multiple particles settling in a toroidal duct with $a_{SCC} = 182\ \mu m$, $R_{SCC} = 3.64$ mm, and $a_p = 15\ \mu m$. To obtain a scenario similar to that in an SCC, we impose the rotation proposed in [44], which mimics a typical head maneuver (Figure 6(a)), and we account for the restoring force of the cupula on the fluid. To do so, we modify ΔP_p by adding a contribution $-\Delta P_\alpha$ due to the inertia of the fluid in the rotating torus and a contribution $-\Delta P_c$ due to the elasticity of the cupula. For a torus, these terms are simply $\Delta P_\alpha = \rho 2\pi R_{SCC}^2 \ddot{\alpha}$ and $\Delta P_c = K V_c$ (see, e.g., [9]), where $\ddot{\alpha}$ is the component of the angular acceleration of the system $\ddot{\boldsymbol{\alpha}} = (0, 0, \ddot{\alpha})$ perpendicular to the canal plane, $K = 7.74$ GPa/m^3 is an estimate for the cupula stiffness, and V_c is the volume of fluid displaced through each cross section of the torus. Moreover, we set $\beta = 1.4\pi$ in (24), as suggested by Van Buskirk *et al.* [1], to neglect the viscous forces in the larger chamber, the utricle, connected to the SCC.

The computations are performed with respect to a reference frame that rotates with the torus. The monopole strength due to a specific particle is defined as

$$\{F_i^{(\xi)}(\mathbf{x}, t)\} = (\rho_p - \rho)\frac{4}{3}\pi a_p^3 (\mathbf{g}_\alpha(t) + \ddot{\boldsymbol{\alpha}}(t) \times \mathbf{Y}_\xi(t)) \tag{29}$$

where $\rho_p = 2700$ g/m^3 and $\rho = 1000$ g/m^3 are the density of the particle and the fluid, respectively, and $\mathbf{g}_\alpha$ is the gravitational acceleration that is measured from the rotating reference frame and is assumed to be in the (x_1, x_2) plane, that is, the canal plane. To avoid particle–particle overlapping, we modify F_i by adding the following repulsive force $\mathbf{B}^{ij}$ between particles i and j:

$$\mathbf{B}^{ij} = \begin{cases} \frac{F_{ref}}{a_p}\left(\frac{R_{ref}^2 - r_{ij}^2}{R_{ref}^2 - 4a_p^2}\right)^2 \mathbf{d}_{ij}, & \text{if } r_{ij} \leqslant R_{ref} \\ (0, 0, 0), & \text{if } r_{ij} > R_{ref}, \end{cases} \tag{30}$$

(a) $t = 0$s: particles at rest, rotation begins

(b) $t = 2.14$s: particles start falling

(c) $t = 3.08$s: settling particles have detached from the wall

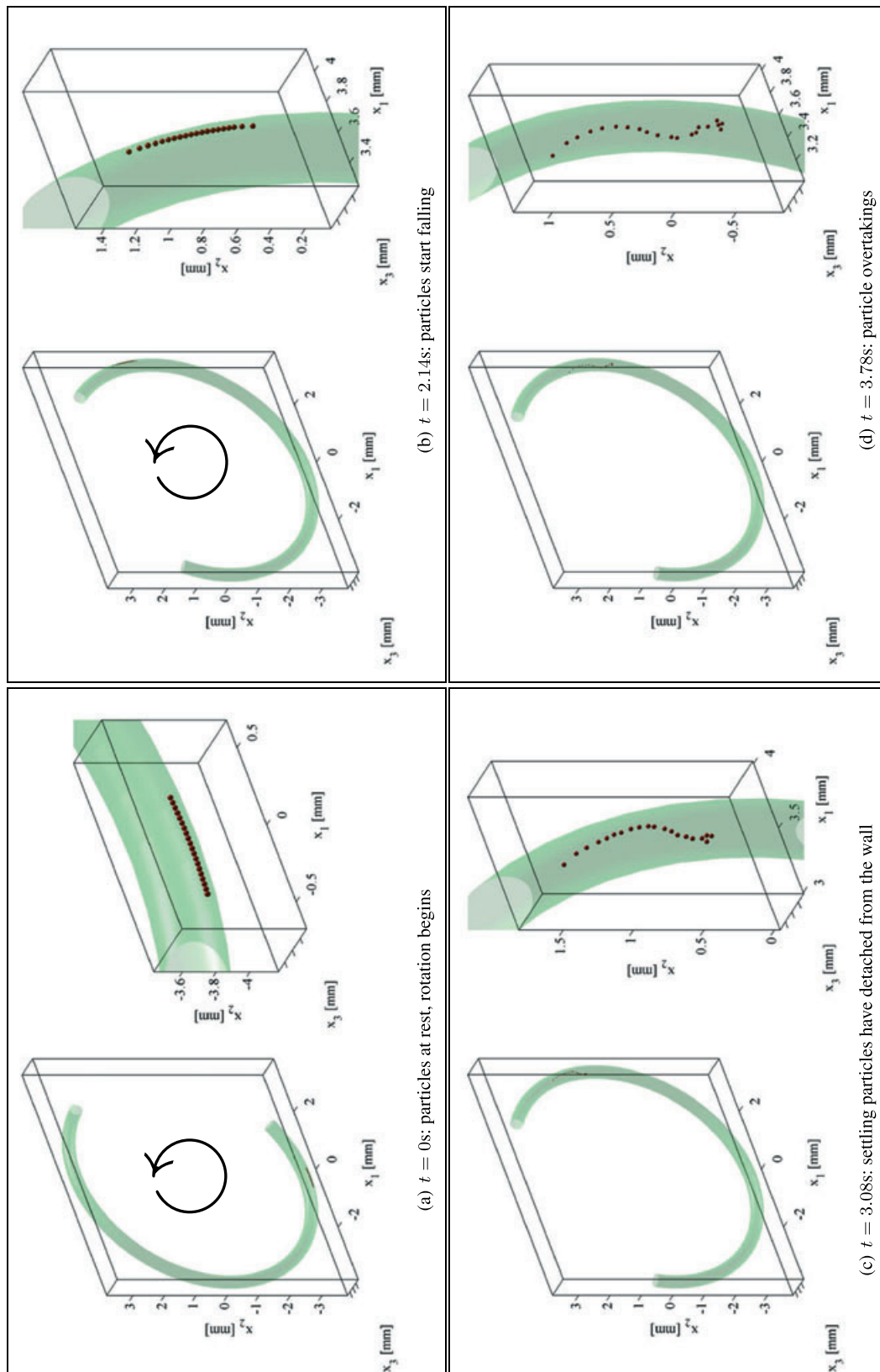(d) $t = 3.78$s: particle overtakings

Figure 5. Illustration of the trajectory of multiple particles (dots) during, (a) and (b), and after, (c) and (d), the rotation. Circular arrows indicate the direction of rotation.
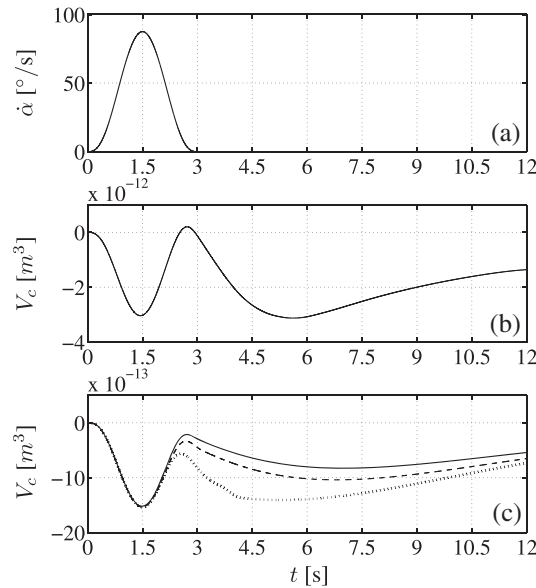
Figure 6. (a) Angular velocity $\dot{\alpha}$ perpendicular to the plane of the canal for a typical head maneuver. (b) and (c) Volume of fluid V_c displaced through the cross sections of the torus during (0 s $\leqslant t \leqslant$ 3 s) and after ($t >$ 3 s) the rotation. (b) corresponds to the simulation illustrated in Figure 5. (c) shows a comparison between a result from [9, Figure 11] (——) and the results from two simulations where the initial distance between the particles is set to $2.2a_p$ (– – –) and $20a_p$ ($\cdots$), respectively.

with the typical force $F_{\text{ref}} = 6 \max (|F_k^{(i)}|, |F_k^{(j)}|)$, the cutoff distance $R_{\text{ref}} = 2.2a_p$, the distance r_{ij} between the particle centers, and the unit vector $\mathbf{d}_{ij} = (\mathbf{Y}_i - \mathbf{Y}_j)/r_{ij}$. A similar repulsive force was previously used by [24] and [18, 25]. For particles close to the wall, we also add a lubrication force such as in [24] precomputed for a single particle.

The particles are initially positioned at the lower part of the canal (Figure 5(a)). During the rotation (0 s $\leqslant t \leqslant$ 3 s), the particles are lifted to a higher position, such that they start falling down toward the end of the head maneuver (Figure 5(b)). After the maneuver ($t >$ 3 s), the particles are still settling, and the trajectory of each particle is influenced by the neighboring particles such that we observe several overtakings and so-called kissing-and-tumbling particles (Figure 5(c) and (d)).

The displaced volume of fluid V_c is shown in Figure 6(b). This volume can be interpreted as the volumetric cupula displacement that leads to the perception of angular motion. During the rotation (0 s $\leqslant t \leqslant$ 3 s), the flow rate is dominated by the contribution of ΔP_α (fluid inertia), which leads to a first cupula displacement that is approximately proportional to the angular velocity $\dot{\alpha}$. After the rotation ($t >$ 3 s), the particles settle along the canal and lead to a second cupula displacement that is believed to be the cause of BPPV with canalithiasis.

In Figure 6(c), we show a comparison with a result reported in [9, Figure 11] for $n_p = 5$ and $a_p = 25$ μm. To allow a direct comparison with the two-dimensional model proposed in [9], we set $R_{\text{SCC}} = 3.2$ mm, $a_{\text{SCC}} = 160$ μm, $K = 13$ GPa/m^3, and $\Delta P_\alpha = \rho(1.82\pi)R_{\text{SCC}}^2\ddot{\alpha}$ (which accounts for the fact that the inertia of the fluid surrounding the cupula was not considered in [9]). The cupula displacement that we obtain with this setting for $n_p = 0$ is almost identical to what has been reported in [9] (not shown). In [9], the particle cluster is modeled as a single heavy particle initially positioned at the lowest point of the SCC. In contrast, we initially position a file of particles (i.e., an actual particle cluster) at the bottom of the canal and repeat the simulation for two values of the initial distance between the particles ($2.2a_p$ and $20a_p$, respectively). The cupula displacements predicted by our model are qualitatively similar to those from [9], but significant quantitative differences are present because of the simplifications in [9]. Moreover, our model predicts changes in the cupula displacement when the initial distance between the particles is changed (Figure 6(c)). These changes are associated to the fact that our model (in contrast to previous ones) can account

for changes in the trajectory of each particle and for the dependency of the settling velocity on the particle–particle distance.

More results for different particle sizes and numbers are reported in [38].

6. DISCUSSION AND FINAL REMARKS

We have proposed a new MFS–FCM coupling for the computation of Stokes flows with particles. This arguably represents the first attempt to couple the FCM to a boundary method. No volumetric mesh is required, which alleviates the constraints on the resolution of a volumetric mesh of the fluid volume occupied by the FCM particle (about five elements per direction [13]). When the particle is far from the boundary, the distance between the collocation points can be even larger than the particle diameter. If the particle touches the boundary, then we obtain a root-mean-square boundary error of less than 1% with about six collocation points per particle diameter. The MFS is also meshless; that is, no information on the connectivity between the collocation points is required. This makes the method easier to program, particularly in complex three-dimensional geometries.

Moreover, we proposed exact MFS quadratures, Equation (22), for the computation of the FCM integrals. These new quadratures do not require the evaluation of the Stokeslets of the MFS expansion such that their computation is approximately n_g^3 times faster than the evaluation of standard Gauss–Hermite quadratures, where n_g is the order of the Hermite polynomial. We also point out that the MFS solution is defined in the whole $\mathbb{R}^3$ space (except for a finite number of singularities) such that the FCM integrals are computed without ambiguities even when the force envelopes overlap the physical boundary. In contrast, methods based on a volumetric mesh require truncating the force envelope and possibly introducing image envelopes to account for the arising error [18].

To demonstrate the applicability of the proposed method, we considered an example of particle-driven flows in a rotating torus with properties similar to a human SCC. We have suggested an efficient and straightforward domain decomposition approach, in which only the flow field in the proximity of the particle is computed numerically, whereas the far field is computed analytically. In this context, we also extended the formula proposed in [8] for the transcupular pressure induced by a singular Stokeslet (infinitesimally small particle) to finite-size multipoles (finite-size particles), Equation (28). The obtained particle trajectories are far more complex than what can be captured by current analytical models. We track the trajectory of each particle. The particles perturb the surrounding fluid such that we can capture the particle–particle and the particles–wall hydrodynamic interactions. Moreover, large particles can also be properly modeled because we account for the finite size of the particle. These features are not included in available models that are limited to a phenomenological description of BPPV and cannot be conclusive on the effect of changes in particle size, number, and position on the cupula displacement. The proposed model will be applied to investigate the phenomena underlying BPPV which available analytical models cannot explain. One example is BPPV fatigue, where particle–particle interactions and particle clusters are suspected to play a major role.

APPENDIX A: DERIVATION OF THE QUADRATURE FORMULAS

The derivations of the new formulas in (22) are based on the reciprocal theorem (RT) [34, 40]. The RT relates two Stokes flows with flow velocities $\mathbf{u}_{1,2}$, stress tensors $\boldsymbol{\sigma}_{1,2}$, and external forces $\mathbf{f}_{1,2}$ as

$$\int_{\partial\hat{\Omega}} \mathbf{n}\cdot\boldsymbol{\sigma}_2\cdot\mathbf{u}_1\,\mathrm{d}^2\mathbf{x} - \int_{\partial\hat{\Omega}} \mathbf{n}\cdot\boldsymbol{\sigma}_1\cdot\mathbf{u}_2\,\mathrm{d}^2\mathbf{x} = -\int_{\hat{\Omega}} \mathbf{f}_2\cdot\mathbf{u}_1\,d\hat{\Omega} + \int_{\hat{\Omega}} \mathbf{f}_1\cdot\mathbf{u}_2\,d\hat{\Omega} \qquad (A.1)$$

where $\hat{\Omega}$ is an auxiliary volume delimited by a surface $\partial\hat{\Omega}$ with the unit normal $\mathbf{n}$.

To derive (22a), we use the RT to compare the MFS solution $\mathbf{u}_{\mathrm{h}}$ with the solution $\mathbf{u}_M$, Equation (14), for an isolated finite-size monopole of strength $F_k = \delta_{ki}$, where i indicates the component of (22a) to be computed. We choose $\hat{\Omega} = \mathbb{R}^3$ such that both $\mathbf{u}_{\mathrm{h}}$ and $\mathbf{u}_M$ go to zero at $\partial\hat{\Omega}$, and we can drop the left-hand side of (A.1) to obtain

$$\int_{\mathbb{R}^3} \Delta_M(\hat{\mathbf{x}}) \, u_{\mathrm{h},i}(\mathbf{x}) \, \mathrm{d}^3\mathbf{x} = \int_{\mathbb{R}^3} \sum_{\xi=1}^{N_s} [w_{\xi,j} \delta(\mathbf{x}-\mathbf{s}_\xi)] \, \hat{S}_{ji}(\hat{\mathbf{x}}) \, \mathrm{d}^3\mathbf{x}. \tag{A.2}$$

The left-hand side of (A.2) is the sought contribution of $\mathbf{u}_\mathrm{h}$ to the particle velocity. The right-hand side of (A.2) can be easily evaluated recalling that $\int_{\mathbb{R}^3} \hat{S}_{ji}(\mathbf{x})\delta(\mathbf{x}-\mathbf{s}) \, \mathrm{d}^3\mathbf{x} = \hat{S}_{ji}(\mathbf{s})$. Substituting (A.2) into (5), we obtain (22a).

Similarly, we can derive (22b) and (22c) by comparing $\mathbf{u}_\mathrm{h}$ with the flow $\mathbf{u}_D$, Equation (18), for an isolated dipole with coefficients $G_{kl} = \delta_{ik}\delta_{jl}$, where i and j can be equal to one, two, or three. The RT becomes

$$\int_{\mathbb{R}^3} u_{\mathrm{h},i}(\mathbf{x}) \frac{\partial}{\partial x_j} \Delta_D(\hat{\mathbf{x}}) \mathrm{d}^3\mathbf{x} = \int_{\mathbb{R}^3} \sum_{\xi=1}^{N_s} [w_{\xi,k} \delta(\mathbf{x}-\mathbf{s}_\xi)] \, R_{kij}(\hat{\mathbf{x}}) \mathrm{d}^3\mathbf{x}. \tag{A.3}$$

The left-hand side of (A.3) can be replaced by the equivalent expression [25]

$$-\int_{\mathbb{R}^3} \frac{\partial u_{\mathrm{h},i}(\mathbf{x})}{\partial x_j} \Delta_D(\hat{\mathbf{x}}) \mathrm{d}^3\mathbf{x}, \tag{A.4}$$

which is the sought contribution of $\mathbf{u}_\mathrm{h}$ to the integral terms $\int_{\mathbb{R}^3} \frac{\partial u_i(\mathbf{x})}{\partial x_j} \Delta_D(\hat{\mathbf{x}}) \, \mathrm{d}^3\mathbf{x}$ in (4) and (6). Evaluating the right-hand side of (A.3) and substituting it into (4) and (6), we obtain (22c) and (22b), respectively.

APPENDIX B: FAR-FIELD PRESSURE DUE TO A MONOPOLE AND A DIPOLE IN A PIPE

To derive (28), we invoke the RT (A.1) and consider (i) the flow induced by a finite-size monopole in an otherwise quiescent fluid inside an infinitely long tube and (ii) the steady pressure-driven flow in an infinitely long tube with mass flow rate Q, velocity $\mathbf{u}_2 = \{u_{2,i}\}$, stress tensor $\boldsymbol{\sigma}_2$, and body force $\mathbf{f}_2 = 0$. Here, the control volume $\hat{\Omega}$ in (A.1) is the actual fluid domain Ω in the tube. Both flows must satisfy the no-slip boundary conditions at the tube wall. Moreover, the finite-size monopole has the same far field as a Stokeslet such that it leads to zero velocity and uniform pressure at the two ends of the tube [45]. Therefore, the left side of (A.1) is reduced to $\Delta P_\mathrm{p} \, Q$, and we have

$$\Delta P_\mathrm{p} \, Q = \int_\Omega F_i \Delta_M u_{2,i} \, \mathrm{d}\Omega \tag{B.1}$$

Replacing the flow $\mathbf{u}_2$ by a Poiseuille flow gives the first term of (28). Similarly, the RT gives the second term of (28) if we compare (i) the flow induced by a finite-size dipole in a pipe and (ii) the Poiseuille flow $\mathbf{u}_2$.

REFERENCES

1. Van Buskirk WC, Watts RG, Liu YK. The fluid mechanics of the semicircular canals. *Journal of Fluid Mechanics* 1976; **78**(01):87–98.
2. Damiano ER, Rabbitt RD. A singular perturbation model of fluid dynamics in the vestibular semicircular canal and ampulla. *Journal of Fluid Mechanics* 1996; **307**(1):333–372.
3. Boselli F, Obrist D, Kleiser L. Vortical flow in the utricle and the ampulla: a computational study on the fluid dynamics of the vestibular system. *Biomechanics and Modeling in Mechanobiology* 2012; **12**(2):335–348. DOI: 10.1007/s10237-012-0402-y.
4. Dix MR, Hallpike CS. The pathology, symptomatology and diagnosis of certain common disorders of the vestibular system. *Proceedings of the Royal Society of Medicine* 1952; **45**(6):341–354.
5. Honrubia V, Bell T, Harris M, Baloh R, Fisher L. Quantitative evaluation of dizziness characteristics and impact on quality of life. *American Journal of Otolaryngology* 1996; **17**(4):595–602.

6. House MG, Honrubia V. Theoretical models for the mechanisms of benign paroxysmal positional vertigo 2003; **8**(Audiology and Neurotology):91–99. DOI: 10.1159/000068998.

7. Rajguru SM, Ifediba MA, Rabbitt RD. Three-dimensional biomechanical model of benign paroxysmal positional vertigo. *Annals of Biomedical Engineering* 2004; **32**:831–846.

8. Squires TM, Weidman MS, Hain TC, Stone HA. A mathematical model for top-shelf vertigo: the role of sedimenting otoconia in BPPV. *Journal of Biomechanics* 2004; **37**(8):1137–1146.

9. Obrist D, Hegemann S. Fluid–particle dynamics in canalithiasis. *Journal of the Royal Society Interface* 2008; **5**(27):1215–1229.

10. Rajguru SM, Rabbitt RD. Afferent responses during experimentally induced semicircular canalithiasis. *Journal of Neurophysiology* 2007; **97**(3):2355–2363. DOI: 10.1152/jn.01152.2006.

11. Valli P, Botta L, Zucca G, Valli S, Buizza A. Simulation of cupulolithiasis and canalolithiasis by an animal model. *Journal of Vestibular Research Equilibrium and Orientation* 2009:89–96.

12. Maxey MR, Patel BK. Localized force representations for particles sedimenting in Stokes flow. *International Journal of Multiphase Flow 9* 2001; **27**(9):1603–1626.

13. Lomholt S, Maxey MR. Force-coupling method for particulate two-phase flow: Stokes flow. *Journal of Computational Physics 1* 2003; **184**(2):381–405.

14. Boselli F, Obrist D, Kleiser L. A multilayer method of fundamental solutions for Stokes flow problems. *Journal of Computational Physics* 2012; **231**:6139–6158. DOI: 10.1016/j.jcp.2012.05.023.

15. Dance SL, Climent E, Maxey MR. Collision barrier effects on the bulk flow in a random suspension. *Physics of Fluids* 2004; **16**(3):828–831. DOI: 10.1063/1.1637349.

16. Liu D, Maxey MR, Karniadakis GE. A fast method for particulate microflows. *Journal of Microelectromechanical Systems* 2002; **11**(6):691–702. DOI: 10.1106/JMEMS.2002.805209.

17. Abbas M, Climent E, Simonin O, Maxey MR. Dynamics of bidisperse suspensions under Stokes flows: linear shear flow and sedimentation. *Physics of Fluids* 2006; **18**(12):121–504. DOI: 10.1063/1.2396916.

18. Yeo K, Maxey MR. Numerical simulations of concentrated suspensions of monodisperse particles in a Poiseuille flow. *Journal of Fluid Mechanics* 2011; **682**:491–518. DOI: 10.1017/jfm.2011.241.

19. Climent E, Yeo K, Maxey MR, Karniadakis GE. Dynamic self-assembly of spinning particles. *Journal of Fluids Engineering Transactions of the ASME* 2007; **129**(4):379–387. DOI: 10.1115/1.2436587.

20. Climent E, Maxey MR, Karniadakis GE. Dynamics of self-assembled chaining in magnetorheological fluids. *Langmuir* 2004; **20**(2):507–513.

21. Liu D, Maxey MR, Karniadakis GE. Modeling and optimization of colloidal micro-pumps. *Journal of Micromechanics and Microengineering* 2004; **14**(4):567–575. DOI: 10.1088/0960-1317/14/4/018.

22. Keaveny EE, Maxey MR. Interactions between comoving magnetic microswimmers. *Physical Review E* 2008; **77**:041–910.

23. Liu D, Keaveny EE, Maxey MR, Karniadakis GE. Force-coupling method for flows with ellipsoidal particles. *Journal of Computational Physics* 2009; **228**(10):3559–3581. DOI: 10.1016/j.jcp.2009.01.020.

24. Dance S, Maxey MR. Incorporation of lubrication effects into the force-coupling method for particulate two-phase flow. *Journal of Computational Physics* 2003; **189**(1):212–238.

25. Yeo K, Maxey MR. Simulation of concentrated suspensions using the force-coupling method. *Journal of Computational Physics* 2010; **229**(6):2401–2421.

26. Fairweather G, Karageorghis A. The method of fundamental solutions for elliptic boundary value problems. *Advances in Computational Mathematics* 1998; **9**(1-2):69–95.

27. Golberg MA, Chen CS. The method of fundamental solutions for potential, Helmholtz and diffusion problems. In *Boundary Integral Methods: Numerical and Mathematical Aspects*, Golberg M (ed.). WIT Press/Computational Mechanics Publications: Boston/Southampton, 1999; 105–176.

28. Young DL, Jane SJ, Fan CM, Murugesan K, Tsai CC. The method of fundamental solutions for 2D and 3D Stokes problems. *Journal of Computational Physics* 2006; **211**(1):1–8.

29. Young DL, Chen CW, Fan CM, Murugesan K, Tsai CC. The method of fundamental solutions for Stokes flow in a rectangular cavity with cylinders. *European Journal of Mechanics - B/Fluids* 2005; **24**(6):703–716.

30. Young DL, Chiu CL, Fan CM, Tsai CC, Lin YC. Method of fundamental solutions for multidimensional Stokes equations by the dual-potential formulation. *European Journal of Mechanics - B/Fluids* 2006; **25**(6):877–893.

31. Tsai CC, Young DL, Lo DC, Wong TK. Method of fundamental solutions for three-dimensional Stokes flow in exterior field. *Journal of Engineering Mechanics* 2006; **132**:317–326.

32. Alves CJS, Silvestre AL. Density results using Stokeslets and a method of fundamental solutions for the Stokes equations. *Engineering Analysis with Boundary Elements* 2004; **28**(10):1245–1252.

33. Ogata H, Amano K. A fundamental solution method for three-dimensional viscous flow problems with obstacles in a periodic array. *Journal of Computational and Applied Mathematics* 2006; **193**(1):302–318.

34. Pozrikidis C. Boundary integral and singularity methods for linearized viscous flow. In *Cambridge Texts in Applied Mathematics*. Cambridge University Press, 1992; Section 2.2, pp. 22–22; Section 1.4, pages 9–13.

35. Schaback R. Adaptive numerical solution of MFS systems. In *The Method of Fundamental Solutions—A Meshless Method*, Chen CS, Karageorghis A, Smyrlis YS (eds). Dynamic Publishers, 2008; 1–27.

36. Boselli F, Obrist D, Kleiser L. Multilayer MFS for Stokes problems. In *Recent Studies in Meshless & Other Novel Computational Methods*, Sarler B, Atluri SN (eds). Tech Science Press: 5805 State Bridge Rd, Suite G108 Duluth, GA 30097-8220, USA, 2010; 71–86.

37. Shigeta T, Young D, Liu CS. Adaptive multilayer method of fundamental solutions using a weighted greedy QR decomposition for the Laplace equation. *Journal of Computational Physics* 2012; **231**(21):7118–7132. DOI: 10.1016/j.jcp.2012.05.036.

38. Boselli F. Fluid dynamics of the balance sense: a computational study based on the multilayer method of fundamental solutions. ETH Zurich, 2012. http://dx.doi.org/10.3929/ethz-a-007591130.

39. Abramowitz M, Stegun IA (eds). *Handbook of Mathematical Functions with Formulas, Graphs, and Mathematical Tables*, Reprint of the 1972 edn. Dover Publications, Inc: New York, 1992.

40. Happel J, Brenner H. *Low Reynolds Number Hydrodynamics with Special Applications to Particulate Media*. Noordhoff international publishing, 1973; 23–57 and 286–357.

41. Wang W, Parker KH. Movement of spherical particles in capillaries using a boundary singularity method. *Journal of Biomechanics* 1998; **31**(4):347–354. DOI: 10.1016/S0021-9290(98)00024-4.

42. Bungay PM, Brenner H. Pressure drop due to the motion of a sphere near the wall bounding a Poiseuille flow. *Journal of Fluid Mechanics* 1973; **60**(01):81–96. DOI: 10.1017/S0022112073000054.

43. Bungay PM, Brenner H. The motion of a closely-fitting sphere in a fluid-filled tube. *International Journal of Multiphase Flow* 1973; **1**(1):25–56. DOI: 10.1016/0301-9322(73)90003-7.

44. Obrist D, Hegemann S, Kronenberg D, Häuselmann O, Rösgen T. In vitro model of a semicircular canal: design and validation of the model and its use for the study of canalithiasis. *Journal of Biomechanics* 2010; **43**(6):1208–1214.

45. Liron N, Shahar R. Stokes flow due to a Stokeslet in a pipe. *Journal of Fluid Mechanics* 1978; **86**(4):727–744.